Frequency domain photothermoacoustic signal amplitude dependence on the optical properties of water: turbid polyvinyl chloride-plastisol system

Gloria M. Spirou,[1,*] Andreas Mandelis,[3,7] I. Alex Vitkin,[2,4,5] and William M. Whelan[2,6]

[1]Department of Medical Physics, McMaster University, Hamilton, Ontario, Canada

[2]Department of Medical Biophysics, University of Toronto, Toronto, Ontario, Canada

[3]Center of Advanced Diffusion-Wave Technologies, Departments of Mechanical and Industrial Engineering, University of Toronto, Toronto, Ontario, Canada

[4]Ontario Cancer Institute/Princess Margaret Hospital/University Health Network, Division of Biophysics and Bioengineering, Toronto, Ontario, Canada

[5]Department of Radiation Oncology, University of Toronto, Toronto, Ontario, Canada

[6]Department of Physics, Ryerson University, Toronto, Ontario, Canada

[7]Institute of Biomaterials and Biomedical Engineering, University of Toronto, Toronto, Ontario, Canada

*Corresponding author: gloria.spirou@gmail.com

Received 18 December 2007; revised 4 April 2008; accepted 5 April 2008; posted 11 April 2008 (Doc. ID 90742); published 2 May 2008

Photoacoustic (more precisely, photothermoacoustic) signals generated by the absorption of photons can be related to the incident laser fluence rate. The dependence of frequency domain photoacoustic (FD-PA) signals on the optical absorption coefficient (μ_a) and the effective attenuation coefficient (μ_{eff}) of a turbid medium [polyvinyl chloride-plastisol (PVCP)] with tissuelike optical properties was measured, and empirical relationships between these optical properties and the photoacoustic (PA) signal amplitude and the laser fluence rate were derived for the water (PVCP system with and without optical scatterers). The measured relationships between these sample optical properties and the PA signal amplitude were found to be linear, consistent with FD-PA theory: $\mu_a = a(A/\Phi) - b$ and $\mu_{\text{eff}} = c(A/\Phi) + d$, where Φ is the laser fluence, A is the FD-PA amplitude, and $a, \ldots, d$ are empirical coefficients determined from the experiment using linear frequency-swept modulation and a lock-in heterodyne detection technique. This quantitative technique can easily be used to measure the optical properties of general turbid media using FD-PAs.

OCIS codes: 120.0120, 110.5125.

1. Introduction

In recent years the field of photoacoustics for imaging has been rapidly developing in biomedical studies [1–12]. The photoacoustic (PA) effect describes sound waves generated due to the interaction of light with a medium. After a photon is absorbed, a PA signal is generated in optically excited systems that undergo nonradiative deexcitation leading to heating and thermoelastic expansion, thus producing ultrasonic waves [1,3,13]. In most studies the main choice for optical illumination is a pulsed laser. Some of the disadvantages of pulsed PA detection include laser

0003-6935/08/142564-10$15.00/0

jitter noise, acoustic and thermal noise within the wide bandwidth of the detector, and strong background signals from sound-scattering tissue [5]. Furthermore, absorbing tissue features located below the surface are hard to detect due to stronger surrounding acoustic reflections being detected simultaneously. These factors limit contrast and signal-to-noise ratio (SNR) and can conceal subtle signals generated from small subsurface absorbers such as nascent cancerous tumors.

We present a frequency domain photoacoustic (FD-PA) study on a system that uses a linear-frequency-modulated (LFM) or chirped laser source and Fourier-spectrum signal acquisition [5,10]. Despite the fact that a more comprehensive LFM experimental configuration capable of subsurface three-dimensional imaging has been developed by our group [14], the measurements of the present study lead to universal relationships among the optical parameters μ_a and μ_{eff}, which are independent of the particulars of the experimental system [5,10].

Advantages of frequency domain biophotoacoustics over pulsed excitation include (1) the tissue is exposed to much lower laser fluence; (2) a coherent data processing algorithm can be utilized to significantly increase SNR and offset the reduction of acoustic pressure amplitude; (3) a direct relationship between time delay of acoustic response and depth of tissue chromophores can be recovered using linear frequency sweeps and heterodyne signal processing; (4) a wide selection of inexpensive diode laser sources is available in the near-infrared (NIR), which makes possible the design of compact devices tailored to specific biochemical composition of tissue; and (5) a potentially superior SNR. Historically FD-PA methods with periodic single-frequency-modulated laser sources have not been actively pursued in imaging applications of turbid media because the amplitude of the laser-induced acoustic waves is typically several orders of magnitude lower than those in pulsed PA systems. Moreover measurements at a single modulation frequency and coherent signal detection fail to provide unambiguous or wide depth information because typical acoustic wavelengths in the MHz frequency range are <1 mm. Therefore alternative (hybrid) schemes of PA generation and detection have been introduced to take advantage of both the high SNR of frequency domain techniques and the simplicity of time-of-flight measurements typical to pulsed methods [5,10,14]. The application of waveforms with linear frequency sweeps helps to avoid ambiguity in depth measurements and dramatically increases the attainable depth range while exhibiting substantial SNR increase and background signal suppression using correlation or heterodyne demodulation methods for signal detection. The concept of using LFM waveforms for depth profilometry finds numerous similarities in radar technology [15]. An example where frequency-swept signals have been successfully utilized for depth profilometry and imaging and compared with their time-domain counterparts is Fourier-domain optical coherence tomography (FD-OCT) [16,17]. It has been shown [18,19] that spectral measurements employed by FD-OCT with a swept laser source demonstrate concrete advantages over the conventional time-domain technique in terms of SNR. Similar SNR advantages are expected in the case of FD-PA.

It is well-known that the PA effect is dependent on the optical absorption coefficient [20] and is influenced by scattering [21]. Our goal is to understand how a frequency-modulated source generates PA signals and how the optical properties of turbid media affect the detected signals. Furthermore a measurement method is presented that allows the PA signals to be related to the sample optical properties and thus be compared to FD-PA theory [5,10].

2. Theory

In biomedical applications, optical properties are used to describe how photons interact with tissue, and acoustic properties are used to describe how sound waves are affected when interacting with tissue. The optical properties determine the generated PA signal intensity, and the acoustic properties of the system affect the magnitude of the acoustic signal detected. Therefore measurement of the optical properties of the probed turbid medium and proof of agreement of the generated signals with FD-PA theory is essential to the assessment of this technique as a quantitative probe of disease such as blood-rich cancerous lesions, which exhibit substantially different optical absorption coefficient (μ_a) and effective attenuation coefficient (μ_{eff}) from healthy tissues in the 650–1100 nm spectral range.

A. Light Propagation

Optical propagation in a turbid medium such as tissue depends on the absorption coefficient $\mu_a(\text{cm}^{-1})$, the scattering coefficient $\mu_s(\text{cm}^{-1})$, and the index of refraction n. Different tissues have different concentrations of chromophores such as hemoglobin, melanin, and water, leading to tissue-specific μ_a values. The scattering of photons in tissue is a result of microscopic changes in the refractive index of, for example, cell membranes and nuclei, leading to changes in the spatial distribution of the photons [22,23]. Furthermore the size of the unit scatterer relative to the light wavelength also affects the scattering of photons. The reduced scattering coefficient $\mu_s'(\text{cm}^{-1})$ is related to the scattering coefficient by the anisotropy factor g, which describes the directional probability of scattering, according to

$$\mu_s' = \mu_s(1-g). \tag{1}$$

The range of g is from -1 to 1[3]. $\mu_{\text{eff}}\,(\text{cm}^{-1})$ is a useful parameter when scattering and absorption are present in a medium:

$$\mu_{\text{eff}} = \sqrt{3\mu_a(\mu_a+\mu_s')}. \tag{2}$$

Tissue optical absorption and scattering properties are wavelength dependent. As a result the optical

penetration depth in tissues varies with wavelength. Within the NIR wavelength region, photons can travel several millimeters to centimeters in tissue providing maximal penetration [3,23].

B. Photoacoustic Generation

If the incident cw photon irradiation is modulated (at a frequency lower than the rate of nonradiative energy conversion), a periodic pressure fluctuation will result with a frequency equal to the light modulation frequency. The pressure change is a result of the temperature fluctuations resulting from the energy transfer [13], and the pressure decreases at frequencies much higher than the nonradiative energy transfer rate [24]. Another possible PA excitation waveform is pulsed-laser energy. Similar to modulated radiation, when short-pulsed-laser energy is absorbed by the medium, a local temperature rise followed by thermal expansion is generated, thereby producing pressure transients [4]. The pressure transients give rise to pressure waves, typically with frequencies from 50 kHz to 5 MHz, which propagate through the medium and are detected as a function of time [25]. Assuming low absorbing media ($\mu_a < 2\,\mathrm{cm}^{-1}$), the detected PA pressure signal ($P(\omega)$) is directly proportional to the optical energy deposition rate according to both the time-domain theory [26] and the FD-PA theory [24]:

$$P(\omega) \propto \Phi\mu_a. \tag{3}$$

Here Φ is the laser fluence ($\mathrm{W/cm^2}$), such that $\Phi\mu_a$ is the rate of volumetrically absorbed photon energy or optical power density ($\mathrm{W/cm^3}$) [27].

C. Sound Propagation

The acoustic properties of tissue dictate when the acoustic signal generated from the PA effect is detected and regulate the reduction in the signal intensity as the acoustic signal travels through tissue. The speed of sound (c) describes the velocity of the acoustic waves throughout tissue. As sound propagates through media, it can be reflected, refracted, and absorbed. The absorption losses are dependent on frequency and increase with the frequency of the acoustic waves. Additional power losses are generated when acoustic waves are scattered from small size particles (comparable to the wavelength of the waves) within the medium. The acoustic attenuation coefficient $\alpha(\mathrm{cm}^{-1})$ describes the loss of acoustic intensity (I) as a function of depth (z) and is expressed as

$$I(z) = I_o \exp(-\alpha z), \tag{4}$$

where I_o is the intensity at zero depth. The acoustic attenuation (α) is the sum of the absorption (α_a) and scattering (α_s) coefficients [28]. Furthermore the PA signal intensity detected varies with the chosen optical wavelength of the source and the acoustic frequency of the detector since optical properties are wavelength dependent and the speed of sound is medium dependent.

3. Materials and Experimental Methods

A. Phantom Materials and Preparation

PVCP samples were used to investigate the relationship between optical properties and the resulting PA signals generated. The procedure described by Spirou *et al.* [29] for PVCP sample preparation was used to obtain the desired optical properties. The PA method was used to measure the optical absorption coefficient, and diffuse reflectance measurements were used to obtain the optical scattering coefficient characteristics of PVCP [29]. PVCP is a nontoxic liquid material that becomes solid when heated to high temperatures of ~200 °C and left to cool down to room temperature. Controlled amounts of black color plastisol (BCP) and titanium dioxide (TiO_2) powder allowed for the desired absorption and reduced scattering coefficients. Because of the high temperature of the PVCP during preparation, obtaining the desired thickness for the samples was difficult. As a result the thickness of the samples slightly varied in these measurements. The diameter of the samples was always larger than their thickness (L) and greater than the optical beam diameter. Furthermore the samples were submerged in a large water tank to provide acoustic coupling.

Table 1 lists the relevant properties of the synthesized samples. The absorbing samples (Sa_1, Sa_2, Sa_3, and Sa_4) were used to study the detected PA signals as a function of μ_a. Since the ability of the system to detect purely absorbing samples was unknown, the range of absorption coefficient values varied from 0.18 to $1.8\,\mathrm{cm}^{-1}$. The high absorption coefficient of $1.8\,\mathrm{cm}^{-1}$ was used to ensure a signal would be detected, then the value was decreased to test the dynamic range of detectable signals. The values chosen correspond to the lower end of absorption values in various human tissues (0.3–$8\,\mathrm{cm}^{-1}$) at 1064 nm [3]. The turbid PVCP samples were used to investigate the effects of scattering on PA signals. With these samples two effects were studied: (1) signal intensity as a function of μ_s' with a constant μ_a, and (2) signal intensity as a function of μ_a with a constant μ_s'. Samples A, B, and C in Table 1 have a similar μ_s' within experimental error, and samples A, D, and E have the

Table 1. Optical Properties of Absorbing Samples (M_A) and Turbid Samples (M_A and $M_{S'}$) and the Thickness L of the Samples

Absorbing samples	L (cm)	μ_a (cm^{-1})	μ_s' (cm^{-1})
Sa_1	1.32 ± 0.05	1.8 ± 0.1	
Sa_2	0.91 ± 0.05	0.91 ± 0.08	
Sa_3	1.06 ± 0.05	0.45 ± 0.04	
Sa_4	0.90 ± 0.05	0.18 ± 0.02	
Turbid samples			
A	1.95 ± 0.05	0.89 ± 0.08	9.4 ± 0.8
B	1.57 ± 0.05	0.45 ± 0.04	10 ± 1.0
C	1.78 ± 0.05	0.18 ± 0.02	8.4 ± 0.8
D	1.67 ± 0.05	0.89 ± 0.08	3.4 ± 0.3
E	1.73 ± 0.05	0.89 ± 0.08	2.2 ± 0.3

same μ_a. The range of values for μ_a and μ_s' of the samples is within the known values in human tissues [3]. Since the PA signal amplitude is directly proportional to the absorption coefficient of the irradiated sample, using low values of μ_a, the lower limit of PA detection in humanlike tissue can be explored. The addition of BCP to PVCP adds a black color to the final appearance of the sample. The addition of TiO_2 changes the sample from a dark absorbing appearance to a turbid appearance. The density of PVCP is similar to that of water. Hence the samples float in the water tank unless they are held down. An aluminum and Plexiglas holder was manufactured to hold the samples in place at the bottom of the water tank. The holder with the sample in place was then submerged in the water tank.

B. Experimental Setup

FD-PA imaging was performed using the setup shown in Fig. 1. The system can be separated into three sections: the optical delivery circuit, the acoustic transducer circuit, and the signal generation circuit.

1. *Optical Delivery Circuit*

A collimated cw ytterbium 1064 nm solid-state fiber laser (YLD-10-LP, IPG Photonics, Oxford, Massachusetts, USA) was used as the laser source. An acousto-optic modulator (AOM: N15180-1.06-GAP, NEOS, West Melbourne, Florida, USA) was used to intensity-modulate the light beam. A lens on the entrance side of the AOM focused the laser beam onto the AOM crystal to maximize the diffraction efficiency of the AOM. Three mirrors were used to direct the laser beam onto the sample. The laser power range was 1–2 W, leading to powers less than ~41 mW on the sample due to losses from the optics and diffraction efficiency of the AOM. The laser has a TEM_{00} mode of operation output-collimated beam with linear polarization. A photodiode (PDA255, THORLABS, North Newton, New Jersey, USA) with a 200 μm pinhole attached to a micrometer stage was used to measure the beam spatial profile at the sample location using 200 μm increments. During this measurement the laser beam was chirp-modulated to account for all power losses due to the AOM efficiency. When a modulation is added to the resonant frequency (180 MHz) of the AOM, the efficiency of the diffracted beam further decreases. Fitting the data to a Gaussian beam profile, an e^{-2} laser beam diameter of 1.81 mm with an error of $\pm$0.04 mm was measured at the target location. In the experimental setup shown in Fig. 1, the 180 MHz radio frequency was superposed with a chirp modulation of 0.1 to 1 MHz and a 1 ms repetition rate using a sinusoidal frequency-swept waveform from a function generator (FG).

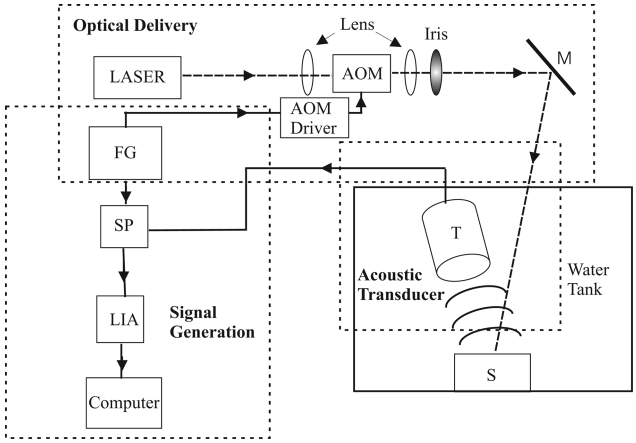

Fig. 1. Schematic of PA imaging system experimental setup: AOM modulator, transducer (T), sample (S), FG , signal processing unit (SP), and mirror (M). The dotted boxes outline the three sections of the experimental setup: optical delivery, acoustic transducer, and signal generation.

Each PVCP sample was illuminated using three fluences (1.0 W/cm^2, 1.5 W/cm^2, and 2.0 W/cm^2), which correspond to the fluence range at the surface of the sample immersed in water. A direct measure of the laser power incident on the sample was not possible because it would require submerging the power meter. Hence the power at the surface location in air was measured, then the sample fluence in water was calculated. To calibrate the data, we measured the power in air first, the power in air through an empty glass-bottom water tank second, and the water tank filled third. Using the Fresnel equations [30]

$$r_{\text{total}} = (r_{\text{TE}}^2 + r_{\text{TM}}^2)/2, \tag{5}$$

where

$$r_{\text{TE}}^2 = \frac{\cos\theta - \sqrt{n^2 - \sin^2\theta}}{\cos\theta + \sqrt{n^2 - \sin^2\theta}},$$
$$r_{\text{TM}}^2 = \frac{n^2\cos\theta - \sqrt{n^2 - \sin^2\theta}}{n^2\cos\theta + \sqrt{n^2 - \sin^2\theta}}, \tag{6}$$

along with the power measurements, the angle of the incident beam ($\theta = 14.1 \pm 0.2)^\circ$, n, the diameter of the beam at the sample location, and the fluence (Φ) at the surface of the sample was calculated for various laser output powers. Errors were propagated throughout all calculations involved to obtain the fluence at the surface of the sample [31].

2. *Acoustic Detector Circuit*

The acoustic wave, generated by the thermomechanical stress in the sample, was detected by the acoustic transducer. A single 28.6 mm diameter element acoustic transducer (V391, Panametrics, Waltham, Massachusetts, USA) with a 50.8 mm focal length, a 0.5 MHz center frequency, and a 0.31 MHz full width at half maximum (FWHM) bandwidth was used to detect the photoacoustic waves, and signals were amplified using two ultrasonic preamplifiers (5662PREAMP and 5676PREAMP, Panametrics, Walthan, Massachusetts, USA).

The pressure signal detected by the transducer contains the same spectral (frequency) content as the chirp-modulated incident laser beam. The complex pressure field generated in an absorbing material as a function of angular frequency (ω) can be expressed as [5]

$$P(\omega;t) = -\omega\rho i_f C_1(\omega) e^{\omega i[t-(d/c_f)]}, \tag{7}$$

where $\omega(t) = 2\pi(a_f + bt)$ is the instantaneous angular frequency, $a_f = 0.1\,\mathrm{MHz}$ is the starting frequency, $b = 0.9\,\mathrm{MHz/ms}$ is the sweep rate of the chirp modulation, ρ_f is the density of the coupling medium (water), d is the distance from the sample to the transducer, and c_f is the speed of sound in the fluid. The constant (C_1) is a complex coefficient obtained from the boundary conditions of the experimental setup [5]:

$$C_1(\omega) = K\mu_a\Psi. \tag{8}$$

Here Ψ is the laser fluence and K is a complex constant dependent on the medium's optical, acoustic, thermal, and elastic properties. A full description of Eq. (8) can be found in Eq. (20) of [5].

From the known dimensions of the transducer, the FWHM focal spot size ($\mathrm{FS_{FWHM}}$) and depth of field (DOF) can be calculated using the following equations [32]:

$$\mathrm{FS_{FWHM}} = 0.7047\lambda_s F_a/a, \tag{9}$$

$$\mathrm{DOF} = 1.85F_a^2\lambda_s/a^2, \tag{10}$$

where $\lambda_s = c_s/f_s$ is the wavelength of sound, c_s is the speed of sound (1493 m/s in water), f_s is the frequency of sound (0.5 MHz), F_a is the acoustic focal length, and a is the radius of the transducer element. Using Eqs. (9) and (10), the DOF of the transducer was determined to be 70 mm with a FWHM focal spot size of 7.5 mm, where $\lambda_s = 2.99\,\mathrm{mm}$ and $a = 14.29\,\mathrm{mm}$. The focal spot size of the transducer limits the lateral resolution to 7.5 mm for scanning of the transducer in two-dimensional imaging applications. However, the imaging resolution of the PA instrument also depends on the laser beam spot size and scanning step size. The large DOF indicates the sensitivity of detection within this range (70 mm) is approximately constant.

The amplitude and the phase of the acoustic signals are highly sensitive to the position of the acoustic transducer. The transducer's angular inclination with respect to the source of the acoustic waves affects the signal intensity. During all the experimental procedures, the transducer position was fixed to obtain maximum signal without obstructing the path of the laser beam. Once the system alignment was optimized, the positions of the mirror and acoustic transducers were locked in place.

3. *Generation Circuit and Lock-In Heterodyne Analysis of Photoacoustic Signals*

The processing circuit involved in signal acquisition as a function of depth is shown in Fig. 2. A detailed description of the process can be found in [5]. The signal processing equipment involved two FGs (FG1 and FG2: DS345, Stanford Research Systems, Sunnyvale, California, USA), a digital delay/pulse generator (DG: DG535, Stanford Research Systems, Sunnyvale, California, USA), two mixers (M1 and M2: ZAD-3, Mini-Circuits, Branson, Missouri, USA), a low-pass filter (LPF: SR640, Stanford Research Systems, Sunnyvale, California, USA) and a lock-in amplifier (LIA: SR844, Stanford Research Systems, Sunnyvale, California, USA).

The DG is the trigger source for FG1 and FG2. The internal trigger rate of the DG was set to 994 Hz, and two output channels, A and B, were used to trigger FG1 and FG2, respectively. (Refer to Fig. 2 as a guide to the signal processing.) Using the DG, a delay time τ between trigger A and trigger B can be introduced. τ is also related to the depth of detected PA waves with the speed of sound as the proportionality constant. The chirp signal generated by both FGs is a sinusoidal function of the form:

$$\begin{aligned} &\mathrm{Chirp} = C\sin(\omega t + \phi),\\ &\omega(t) = 2\pi f_s(t) = 2\pi(a_f + bt), \end{aligned} \tag{11}$$

where ϕ is the phase and C is the amplitude of the chirp signal. The chirp signal from FG1 modulates the laser beam creating a chirped PA signal when the laser beam interacts with the sample. The chirped PA pressure signal detected by the transducer is delayed due to the finite speed of sound of the PA waves in the sample and the water. This delay is described by

$$S_1 = C(z)\sin\{[a_f + b(t - z/c_s)]t + \phi_1\}, \tag{12}$$

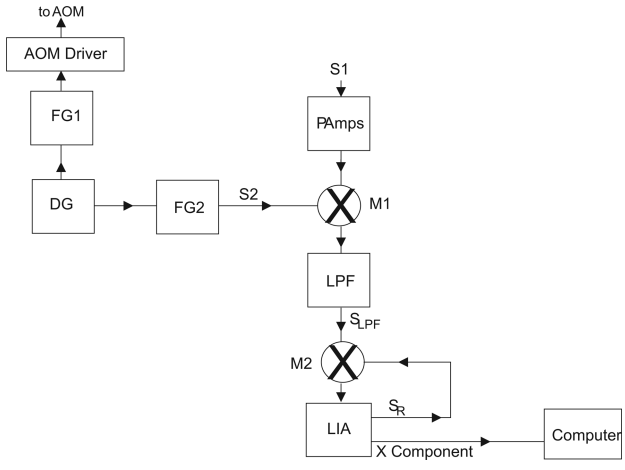

Fig. 2. Signal processing setup: AOM modulator, FG, DG, M1, M2, preamplifiers (PAmps), LPF, and LIA. S_1 is the PA waves detected by transducer, S_2 is the function-generated chirp signal, S_{LPF} is the low-pass-filtered signal, and S_R is the reference signal.

where S_1 is the PA signal intensity, z is the distance from the transducer, c_s is the speed of sound in the solid, ϕ_1 is the phase of the signal, and z/c_s is the acoustic delay time. The signal detected by the transducer is not only frequency modulated, but is also amplitude modulated because C is a function of z. To simplify the signal generation analysis, Eq. (12) is used to represent the acoustic pressure signal instead of Eq. (7). M1 is used to multiply S_1 with a 1 V amplitude chirp signal, S_2. S_2 is generated by FG2 and has a manually selected delay time τ and phase ϕ_2. (Note that $S_2 = \sin\{[a_f + b(t-\tau)]t + \phi_2\}$.) The next step in the signal generation is the multiplication of these two chirp signals ($S_1 \times S_2$) using frequency mixer M1 as shown in Fig. 2. After M1, the signal is low-pass filtered and the high frequencies are removed keeping only the dc and low frequencies (cutoff value of 100 kHz) of the mixed output signal $S_1 \times S_2$:

$$S_{\mathrm{LPF}} = C(z)\cos\{[b(\tau - z/c_s)t] + \Delta\phi_{12}\}, \qquad (13)$$

where $\Delta\phi_{12} = \phi_1 - \phi_2$. To detect the desired S_{LPF} signal, a lock-in heterodyne scheme is used in which the signal is further mixed (using M2) with a reference frequency signal $S_R = \sin(\omega_o t)$, where $\omega_o = 2\pi f_o$ is the LIA internal reference angular frequency with f_o set at 4 MHz. The reference angular frequency was set at 4 MHz to ensure there is no interference between the detected acoustic frequency range (0.1–1 MHz) and the LIA reference angular frequency. The two inputs to M2 are S_{LPF} and S_R. The output of M2 is low-pass filtered using the LIA internal filter, and the only incoming signal the LIA will detect is a signal with the reference frequency, ω_o. The use of a LIA allows for the quick detection of the PA signals (S_{LPF}) as τ is varied. The only M2 signal output with a frequency ω_o occurs when $\tau - z/c_s = 0$ in Eq. (13). From this conclusion, Eq. (13) shows that S_{LPF} contains a dc signal when $\tau = z/c_s$. (The dc signal detected is related to z since τ and c_s are known parameters.) This signal is equal to

$$S_{\mathrm{LPF}} = C(z)\cos[\Delta\phi_{12}(z)]. \qquad (14)$$

This is the signal that is detected by the LIA after M2. This signal contains amplitude and phase components that cannot be separated by the LIA. Thus the signal amplitude detected by the LIA is a real (not complex) signal, a combination of the amplitude and the phase of the PA signals detected. Although a phase was detected by the LIA, it was shown that this phase is an instrumental result of the mixing process through M2 and does not contain any information related to the PA signals. To verify this effect, a dc signal was input to the mixer along with the reference signal from the LIA and the output was connected to the LIA. The LIA detected a phase as a function of the voltage of the input dc signal. It is believed that the observed phase is the result of dc-level differences across various interconnected pathways of the electric circuit in Fig. 2.

4. Computational and Data Analysis

MATLAB (version 6.1, Natick, Massachusetts, USA) was used to collect the LIA information and control the DG. A block diagram of the algorithm used to store and graphically display the data is shown in Fig. 3(a). The user defines the number of depth scans, the starting delay time, the final delay time (τ), and the delay time increment Δt, where Δt ranges from the start delay time to the final delay time τ of the DG. Next the internal trigger source of the DG was set to 994 Hz and paused for 2 s before continuing. This rate was used to trigger the chirp signals generated by FG1 and FG2. The 2 s pause is necessary to allow the DG to stabilize its internal trigger source. Once the trigger rate of the DG is set, data acquisition begins. The program controls the increase in τ by Δt on the DG, which is operator specified. At each τ the X component and phase of the signal detected by the LIA is stored. Once the entire delay range has been scanned, the data are displayed as a graph with the measured X component as function of τ. A typical display is shown in Fig. 3(b). The time constant of the LIA was set to 30 ms to obtain optimal signal intensity at each τ. At each τ setting of the DG, a 30 ms pause was introduced in the algorithm before the data were stored to allow the LIA to stabilize.

The algorithm shown in Fig. 3(a) was used to obtain the optimal Δt of the system. Since τ is related to the depth of the PA signal by $z = \tau c_s$, where c_s in-

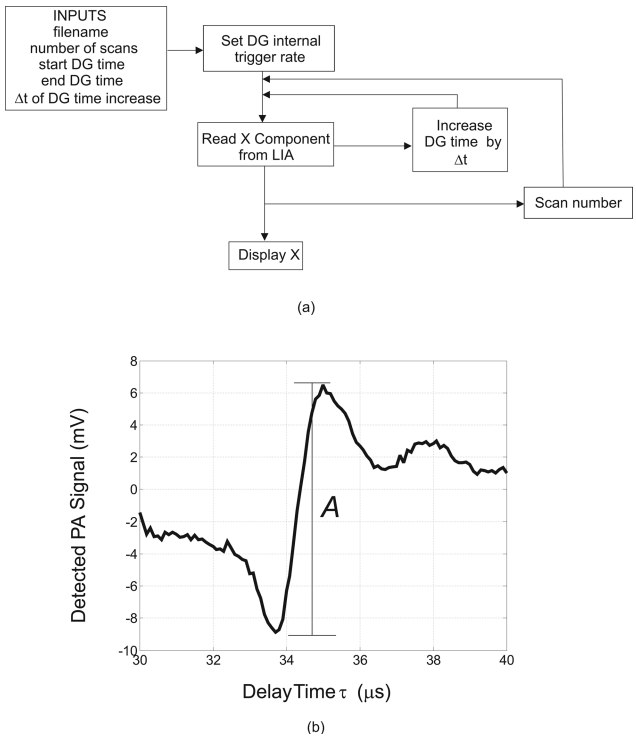

Fig. 3. (a) Block diagram of the procedure used to acquire the FD-PA signal intensity detected by the LIA. (b) Display of PA signal intensity of a sample as a function of τ obtained by the algorithm shown in (a). An example of the FD-PA amplitude A is shown in (b).

cludes the coupling medium, the depth increment of the system was defined by

$$\delta z = \Delta t c_s, \qquad \Delta t > 0.1\,\mu s,$$
$$\delta z = (0.1\,\mu s)c_s, \qquad \Delta t \le 0.1\,\mu s, \tag{15}$$

where Δt is the operator-selected delay time increment. A Δt of 100 ns was observed to be the most efficient given that smaller values did not alter the detected signal, but increased the acquisition time. It was observed that although the signal pattern was altered from one scan to the next due to instrumental limitations with respect to the inability to lock the phases of the two FGs, the amplitude (A) at the surface location was reproducible. An example of the FD-PA A is shown in Fig. 3(b). To better interpret the experimental observations, a simulation model was generated. Equation (7) was multiplied with a simulated signal of the same waveform as Eq. (11), then low-pass filtered. Simulated PA signals were generated by varying τ from 0 to 50 μs in increments of $\Delta t = 0.1\,\mu$s [33]. A for each simulated and measured signal was determined. From both sets of data, it was shown A from all signals was to within 6%. This finding was used to compare PA signals acquired from different samples with different optical properties. Once the time-delay region of interest was selected, our algorithm calculated the amplitude of the PA signal generated near the surface and was used for signal analysis. Since the PA signal is dependent on optical properties, A measured is also related to the optical properties and was used to explore signal dependence on these properties.

5. Results

A. Photoacoustic Signal Intensity in Optically Absorbing (Nonturbid) Media

To investigate the PA signal response as a function of optical absorption, A values were obtained from four different absorbing samples. A value for each sample was the average of several scans. All standard deviations were recorded. A values as a function of fluence with the optical absorption coefficient as a parameter and corresponding straight line weighted fits [31] are shown in Fig. 4(a). It is clear that A values increase linearly with fluence. Figure 4(b) displays A as a function of the optical absorption coefficient with fluence as a parameter. A linear trend between A and μ_a is observed. Although a zero intercept is expected for A when $\mu_a = 0\,\mathrm{cm}^{-1}$, the linear fit was not forced through the origin due to the presence of background noise. Furthermore the intercepts obtained from the fits have a value of zero within the error range (see Fig. 4 caption). In the limit of an optically transparent medium such that $\mu_a \ll |\sigma_s|^{-1}$ and $\mu_a \ll k_s^{-1}$, where $\sigma_s = \sqrt{i\omega/\alpha_s}$ and $k_s = \omega/c_s$ are the thermal and acoustic wavenumbers, respectively (α_s: thermal diffusivity of the solid), the FD-PA theory [Eqs. (21) and (23) of [5]] predicts a linearized amplitude:

$$A = |P(\omega)| \propto |C_1(\omega)| \propto \Phi\mu_a. \tag{16}$$

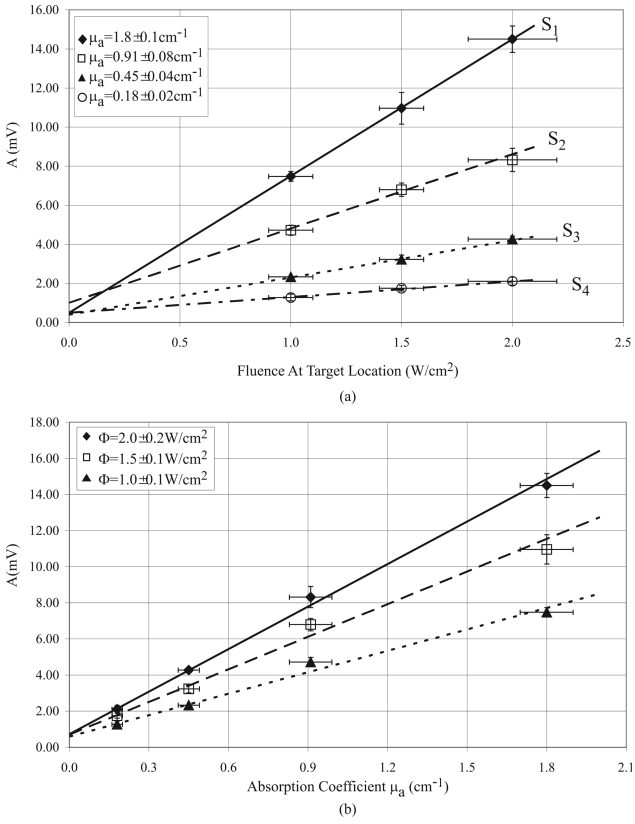

Fig. 4. A signal amplitude in mV (a) as a function of Φ and (b) as a function of μ_a for the four different absorbing samples (Sa_1, Sa_2, Sa_3, and Sa_4 in Table 1). In (a) the lines of best fit for each sample are represented by $A = (7.0 \pm 0.6)\Phi + (0.5 \pm 2.1)$, $A = (3.8 \pm 0.9)\Phi + (1.0 \pm 1.3)$, $A = (1.9 \pm 0.4)\Phi + (0.4 \pm 0.6)$, and $A = (0.8 \pm 0.3)\Phi + (0.5 \pm 0.5)$ for absorbing samples Sa_1, Sa_2, Sa_3, and Sa_4, respectively.

The relationships in Eq. (16) can be expressed in terms of μ_a to yield

$$\mu_a \propto A/\Phi. \tag{17}$$

These proportionalities are borne out by the experimental results: Fig. 5 displays μ_a in cm^{-1} as a function of the ratio of A/Φ (in $\mathrm{mVcm}^2/\mathrm{W}$). From this relationship it is observed that an absolute value for μ_a in PVCP–BCP samples can be obtained as a function of fluence using the empirical expression

$$\mu_a = (0.25 \pm 0.05)(A/\Phi) - (0.03 \pm 0.10)\,[\mathrm{cm}^{-1}]. \tag{18}$$

The linear relationship of Eq. (18) is valid for general water–absorbing (nonturbid) solid interfaces as indicated in the proportionality of Eq. (17). However, the particular coefficients are the result of best fitting the experimental curve to a straight line and are only valid for a water–PVCP sample boundary.

B. Photoacoustic Signal Intensity in Optically Absorbing and Scattering (Turbid) Media

A values for turbid PVCP samples, having similar μ_s' and different μ_a values, were also evaluated. The re-

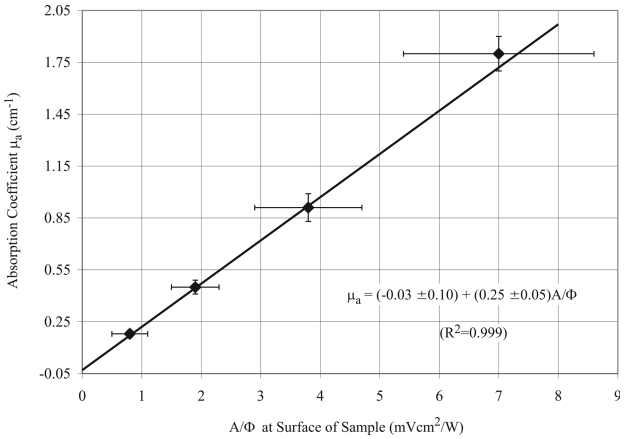

Fig. 5. Relationship between (A/Φ) (mVcm^2/W) and μ_a(cm^{-1}). The solid line is a weighted fit to the data points and is expressed by Eq. (17). The R^2 value is an indicator of the goodness of fit.

sults are shown in Fig. 6(a). It is observed that for an approximately constant optical scattering coefficient, A value increases linearly with the optical absorption coefficient. This is expected from the PA theory of turbid media [Eqs. (3) and (27) of [10]]. In the limit of an optically transparent medium, considerations similar to those discussed above yield

$$A = |P(\omega)| \propto |G_7(\omega)| \propto \Phi\mu_{\text{eff}}, \tag{19}$$

where μ_{eff} is given by Eq. (2). The relationships in Eq. (19) can be expressed in terms of μ_{eff} to yield

$$\mu_{\text{eff}} \propto A/\Phi. \tag{20}$$

The data for samples Sa_2, A, D, and E listed in Table 1 are displayed in Fig. 6(b). These four samples have approximately the same μ_a and varying μ_s'. From this graph it is observed that the introduction of optical scattering to the sample increases the PA signal generated near the surface of the sample. This confirms that the presence of scattering increases the optical fluence near the surface of the target, leading to more highly localized absorption near the surface compared with the absence of optical scattering and is consistent with expected optical trends in turbid media [3,10]. Unfortunately in the turbid media, the optical scattering is increased leading to higher background noise levels of the PA signal. Although the fits were not forced through the origin, the intercept values go through the origin within the error range. As a result the presence of noise may limit the ability to obtain reliable measurements for the effective attenuation coefficient with values close to 0 cm^{-1}.

Calculating the effective optical attenuation coefficient μ_{eff} of the samples listed in Table 1 through best fits using Eq. (2), the relationship between (A/Φ) and μ_{eff} expected from Eq. (20) was obtained as shown in Fig. 7:

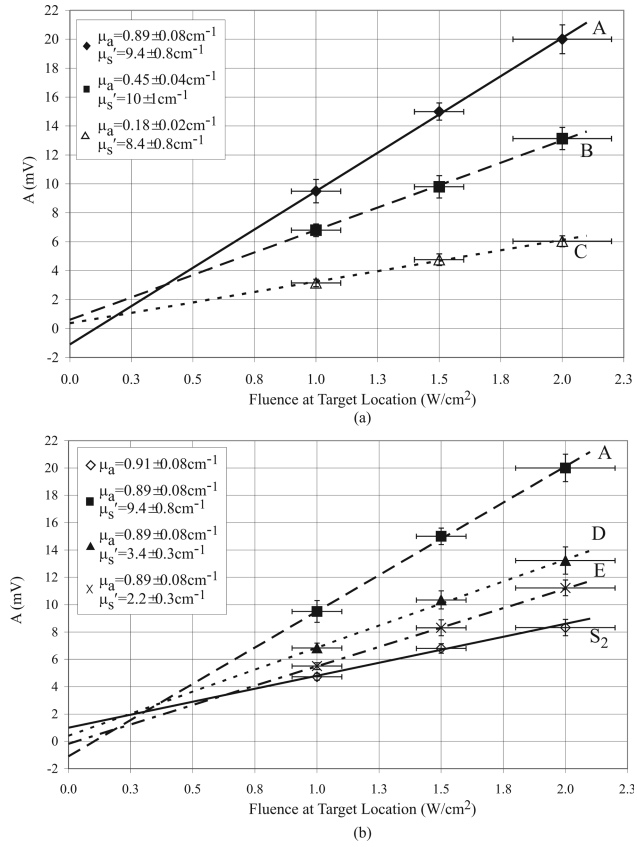

Fig. 6. A (mV) as a function of absorption and scattering coefficients. The straight line fits were obtained by fitting the data to a weighted fit for a straight line error analysis model. (a) The data for samples A, B, and C in Table 1 with similar scattering ($\mu_s' \sim 9.3\,\text{cm}^{-1}$) are displayed. (b) The data for samples A, D, E, and Sa_2 are displayed (see Table 1 for optical properties). The lines of best fit for all the samples in (a) are $A = (10.6 \pm 2.5)\Phi + (-1.1 \pm 3.5)$, $A = (6.2 \pm 1.5)\Phi + (0.6 \pm 2.1)$, and $A = (2.9 \pm 0.8)\Phi + (0.4 \pm 1.1)$ for samples A, B, and C, respectively. The lines of best fit for all the samples in (b) are $A = (3.8 \pm 0.9)\Phi + (1.0 \pm 1.3)$, $A = (10.6 \pm 2.5)\Phi + (-1.1 \pm 3.5)$, $A = (6.5 \pm 1.5)\Phi + (0.4 \pm 2.0)$, and $A = (5.7 \pm 1.3)\Phi + (-0.2 \pm 1.7)$ for samples Sa_2, A, D, and E, respectively.

$$\mu_{\text{eff}} = (0.39 \pm 0.12)(A/\Phi) + (0.99 \pm 0.63)\,[\text{cm}^{-1}]. \tag{21}$$

The linear relation displayed in Fig. 7 describes findings similar to Eq. (18). Equation (21) demonstrates that the absolute value of μ_{eff} for PVCP samples can be obtained with the knowledge of the fluence rate and A values. Again the linear Eq. (21) is valid for general water–turbid solid interfaces, but the particular coefficients are only valid for a water–turbid PVCP sample interface. Besides validating the FD-PA theory, an important value of the empirical Eqs. (18) and (21) can be used to measure μ_a of an absorbing sample and μ_{eff} of a turbid sample, respectively [33].

6. Discussion

A FD-PA study of signal dependence on optical properties of turbid and nonturbid media was conducted. The study relates the detected FD-PA signals to the

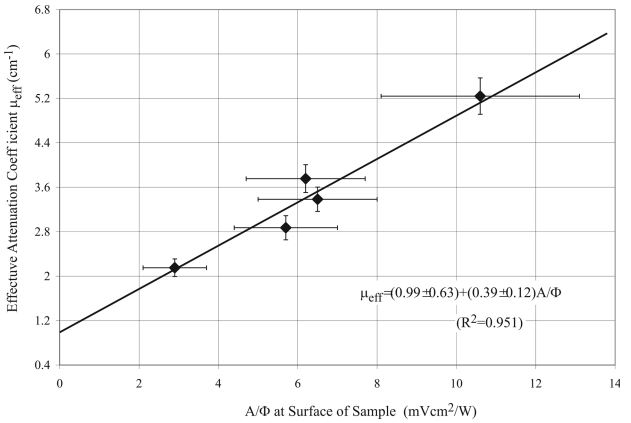

Fig. 7. Relationship between μ_{eff} (cm^{-1}) and (A/Φ) (mVcm^2/W). The solid line is a weighted fit to the data points and is expressed by Eq. (17). The R^2

optical properties (μ_a and μ_{eff}) of the target. A was found to be a meaningful quantity for measuring the effects of absorption and scattering in the PA signals with a standard deviation of 6% between phase-variable PA signals. It is well-known that the sample optical absorption and scattering properties and incident radiation are related to the FD-PA signal amplitude [5,10]. Once the fluence at the surface of the sample is known, a linear relationship between the optical properties of the sample and A/Φ can be deduced and used for these measurements. Linear trends between optical properties and transients in time-domain PA measurements have also been observed by Spirou *et al.* [29] and Oraevsky *et al.* [27]. Potential limitations of this type of empirical linear relationships between optical parameters of the sample and laser parameters are errors arising from the fabrication of the samples and inherent PA signal fluctuations. The relationships described by Eqs. (18) and (21) are generally validated through the FD-PA theory applied to low-μ_a turbid and nonturbid media. However, for a water–solid interface, the associated coefficients must be measured through best fits to curves like those shown in Figs. 5 and 7. Therefore the relationships obtained in Eqs. (18) and (21) can be used for the respective water–solid interfaces toward the measurement of μ_a or μ_{eff} of arbitrary concentrations of the absorber or the scatterer in the solid, an otherwise difficult task that requires integrating spheres and specific theoretical scattering models [3]. Continuing research in Monte Carlo, modeling has led to the ability to retrieve the optical properties μ_a and μ_s' if μ_{eff} of the sample can be measured. This method is described in [34] and the references therein.

The characteristics of the 0.5 MHz acoustic transducer limit the lateral resolution of the system. The focal spot is dependent on the wavelength of sound due to diffraction: the higher the detection frequency of the transducer, the smaller the focal spot. In PAs the higher the modulation frequency of the incident radiation, the lower the thermal penetration (diffusion) length [13]. Thus to increase the resolution of the transducer, an increase in its frequency bandwidth is necessary, which leads to a lower penetration depth and thus a lower detection depth. Furthermore the DOF of the transducer also decreases as the frequency bandwidth of the transducer increases, resulting in smaller regions of constant signal. One of the advantages of using a chirp-modulated beam is the ability to vary the frequency of the modulated beam leading to an increase in sample information contained in various frequencies. A compromise may be found through the use of a wide-band transducer with similar properties to the one utilized in the pulsed PA system (LOIS) [27] or a detector with a varying focal length and increasing the chirp frequency content to increase signal information. The advantage of using a low-frequency transducer was the increase in depth penetration and signal dynamic range. Using the 0.5 MHz transducer, signals from a depth of up to 60 mm were detected. The depth penetration depends on the speed of sound in the sample material and the DOF of the transducer.

7. Conclusions

FD-PA quantitative measurements involving absorption and scattering coefficients of turbid and nonturbid PVCP samples revealed linear relationships between these sample optical properties (and indirectly between the reduced scattering coefficient μ_s' and cosine of the scattering angle g and the signal amplitude/fluence ratios, consistent with FD-PA theory: $\mu_a = a(A/\Phi) - b$ and $\mu_{\text{eff}} = c(A/\Phi) + d$, where Φ is the laser fluence, A is the FD-PA amplitude, and $a, \ldots, d$ are empirical coefficients determined from the experiment using linear-frequency-swept modulation and a lock-in heterodyne detection technique. This quantitative method can be used to obtain the optical properties of unknown samples and of samples with unknown absorber and scatterer concentrations. They can also be used to distinguish intrasample regions with different optical properties.

The authors acknowledge S. Telenkov for his work on the simulated signals. Funding through the Collaborative Health Research Program (CHRP) of National Sciences and Engineering Research Council of Canada awarded to A. Mandelis and I. A. Vitkin is gratefully acknowledged. The awarding of the Scace Prostate Fellowship to G. Spirou, which made this research possible, is gratefully acknowledged. W. Whelan acknowledges the support of the National Cancer Institute of Canada (with funds from the Canadian Cancer Society).

References

1. A. A. Oraevsky and A. A. Karabutov, "Optoacoustic tomography," in *Biomedical Photonics Handbook*, T. Vo-Dinh, ed. (CRC Press, 2003), pp. 34.1–34.34.
2. A. A. Karabutov and A. A. Oraevsky, "Time-resolved detection of optoacoustic profiles for measurement of optical energy distribution in tissues," in *Handbook of Optical Biomedical Diagnostics*, V. V. Tuchin, ed. (SPIE, 2002), pp. 587–646.
3. W. M. Star, B. C. Wilson, A. J. Welch, and M. J. C. van Gemert, *Optical-Thermal Response of Laser-Irradiated Tissue*, A. J.

Welch and M. J. C. van Gemert, eds. (Plenum, 1995), Chaps. 1 and 2.
4. V. E. Gusev and A. A. Karabutov, *Laser Optoacoustics* (AIP, 1993).
5. Y. Fan, A. Mandelis, G. M. Spirou, and I. A. Vitkin, "Development of a laser photothermoacoustic frequency-swept system for subsurface imaging: theory and experiment," J. Acoust. Soc. Am. **116**, 3523–3533 (2004).
6. X. Wang, Y. Pang, G. Ku, G. Stoica, and L. V. Wang, "Three-dimensional laser-induced photoacoustic tomography of mouse brain with the skin and skull intact," Opt. Lett. **28**, 1739–1741 (2003).
7. R. G. M. Kolkman, E. Hondebrink, W. Steenbergen, T. G. van Leeuwen, and F. F. M. de Mul, "Photoacoustic imaging of blood vessels with a double-ring sensor featuring a narrow angular aperture," J Biomed. Opt. **9**, 1327–1335 (2004).
8. R. I. Siphanto, R. G. M. Kolkman, A. Huisjes, M. C. Pilatou, F. F. M. de Mul, W. Steenbergen, and L. N. A. van Adrichem, "Imaging of small vessels using photoacoustics: an in vivo study," Lasers Surg. Med. **35**, 354–362 (2004).
9. G. M. Spirou, I. A. Vitkin, B. C. Wilson, W. M. Whelan, P. M. Henrichs, K. Mehta, T. Miller, A. Yee, J. Meador, and A. A. Oraevsky, "Development and testing of an optoacoustic imaging system for monitoring and guiding prostate cancer therapies," Proc. SPIE **5320**, 44–56 (2004).
10. Y. Fan, A. Mandelis, G. M. Spirou, I. A. Vitkin, and W. M. Whelan, "Laser photothermoacoustic frequency swept heterodyned lock-in depth profilometry in turbid tissue phantoms," Phys. Rev. E **72**, 051908 (2005).
11. G. Ku, X. Wang, X. Xie, G. Stoica, and L. V. Wang, "Imaging of tumor angiogenesis in rat brains *in vivo* by photoacoustic tomography," Appl. Opt. **44**, 770–775 (2005).
12. S. Manohar, A. Kharine, J. C. G. van Hespen, W. Steenbergen, and T. G. van Leeuwen, "The twente photoacoustic mammoscope: system overview and performance," Phys. Med. Biol. **50**, 2543–2557 (2005).
13. A. Rosencwaig, *Photoacoustics and Photoacoustic Spectroscopy* (Robert E. Krieger, 1990).
14. S. A. Telenkov and A. Mandelis, "Fourier-domain biophotoacoustic subsurface depth selective amplitude and phase imaging of turbid phantoms and biological tissue," J. Biomed. Opt. **11**, 044006 (2006).
15. E. C. Farnett and G. H. Stevens, *Radar Handbook*, M. I. Skolnik, ed. (McGraw-Hill, 1990).
16. A. F. Fercher, C. K. Hitzenberger, G. Kamp, and S. Y. El-Zaiat, "Measurement of intraocular distances by backscattering spectral interferometry," Opt. Commun. **117**, 43–48 (1995).
17. G. Hausler and M. W. Lindner, "'Coherence radar' and 'spectral radar'—new tools for dermatological diagnosis," J. Biomed. Opt. **3**, 21–31 (1998).
18. M. A. Choma, M. V. Sarunic, C. Yang, and J. A. Izatt, "Sensitivity advantage of swept source and Fourier domain optical coherence tomography," Opt. Express **11**, 2183–2189 (2003).
19. R. Leitgeb, C. K. Hitzenberger, and A. F. Fercher, "Performance of Fourier domain vs. time domain optical coherence tomography," Opt. Express **11**, 889–894 (2003).
20. A. Rosencwaig and A. Gersho, "Theory of the photoacoustic effect with solids," J. Appl. Phys. **47**, 64–69 (1976).
21. P. Helander, "Theoretical aspects of photoacoustic spectroscopy with light scattering samples," J. Appl. Phys. **54**, 3410–3414 (1983).
22. B. C. Wilson, *Encyclopedia of Human Biology*, R. Dulbecco, ed. (Academic, 1991), pp. 587–597.
23. A. Roggar, K. Dorelschel, O. Minet, D. Wölf, and G. Müller, *Laser-Induced Interstitial Thermotherapy*, G. J. Muller and A. Roggan, eds. (SPIE, 1995), Chap. 10.
24. A. Mandelis and B. S. H. Royce, "Relaxation time measurements in frequency and time-domain photoacoustic spectroscopy of condensed phases," J. Opt. Soc. Am. **70**, 474–480 (1980).
25. V. G. Andreev, A. A. Karabutov, and A. A. Oraevsky, "Detection of ultrawide-band ultrasound pulses in optoacoustic tomography," IEEE Trans. Ultrason. Ferroelectr. Freq. Control **50**, 1383–1390 (2003).
26. S. Manohar, A. Kharine, J. C. G. van Hespen, W. Steenbergen, and T. G. van Leeuwen, "Photoacoustic mammography laboratory prototype: imaging of breast tissue phantoms," J. Biomed. Opt. **9**, 1172–1181 (2004).
27. A. A. Oraevsky, S. L. Jacques, and F. K. Tittel, "Measurement of tissue optical properties by time-resolved detection of laser-induced transient stress," Appl. Opt. **36**, 402–415 (1997).
28. P. Fish, *Physics and instrumentation of diagnostic medical ultrasound* (Wiley, 1990).
29. G. M. Spirou, A. A. Oraevsky, I. A. Vitkin, and W. M. Whelan, "Optical and acoustic properties at 1064 nm of polyvinyl chloride-plastisol for use as a tissue phantom in biomedical optoacoustics," Phys. Med. Biol. **50**, N141–N153 (2005).
30. F. L. Pedrotti and L. S. Pedrotti, *Introduction to Optics*, 2nd ed. (Prentice-Hall, 1993).
31. J. R. Taylor, *An Introduction to Error Analysis*, 2nd ed. (University Science, 1982).
32. T. L. Szabo, *Diagnostic Ultrasound Imaging: Inside Out* (Elsevier, 2004).
33. G. M. Spirou, A. Mandelis, I. A. Vitkin, and W. M. Whelan, "A calibration technique for frequency domain photothermoacoustics," Euro. Phys J. Spec. Top. **153**, 491–495 (2008).
34. L. C. L. Chin, A. E. Worthington, W. M. Whelan, and I. A. Vitkin, "Determination of the optical properties of turbid media using relative interstitial radiance measurements: Monte Carlo study, experimental validation, and sensitivity analysis," J. Biomed. Opt. **12**, 064027 (2007).